JOURNAL OF APPLIED PHYSICS **102**, 063514 (2007)

Multimillion-atom nanoindentation simulation of crystalline silicon carbide: Orientation dependence and anisotropic pileup

Hsiu-Pin Chen, Rajiv K. Kalia, Aiichiro Nakano, and Priya Vashishta[a)]
Collaboratory for Advanced Computing and Simulations, Department of Chemical Engineering and Materials Science, Department of Physics and Astronomy, and Department of Computer Science, University of Southern California, Los Angeles, California 90089-0242, USA

Izabela Szlufarska
Department of Materials Science and Engineering, University of Wisconsin—Madison, Wisconsin 53706-1595, USA

(Received 27 April 2007; accepted 27 July 2007; published online 24 September 2007)

We have performed multimillion-atom molecular dynamics simulations of nanoindentation on cubic silicon carbide (3C-SiC) surfaces corresponding to three different crystallographic directions, (110), (001), and (111), using pyramidal-shaped Vickers indenter with 90° edge angle. Load-displacement (P-h) curves show major and minor pop-in events during loading. Detailed analysis of the (110) indentation shows that the first minor discontinuity in the P-h curve is related to the nucleation of dislocations, whereas the subsequent major load drops are related to the dissipation of accumulated energy by expansion of dislocation loops and changes of slip planes. Motion of dislocation lines in the indented films involves a kink mechanism as well as mutually repelling glide-set Shockley partial dislocations with associated extension of stacking faults during the expansion of dislocation loops. Our simulations provide a quantitative insight into the stress distribution on slip planes and stress concentration at kinks and dislocation cores. The estimated Peierls stress is 7.5 GPa $\approx 3.9 \times 10^{-2} G$, where G is the shear modulus. We find that similar deformation mechanisms operate during nanoindentation of the three surfaces but the calculated hardness values are different, the highest being 27.5 GPa for the (111) plane. Anisotropic pileup patterns are observed after the indenter is unloaded and they all reside on (111) and $(\bar{1}\bar{1}1)$ slip planes. These patterns are closely related to dislocation activities on the two slip planes. The anisotropy is a consequence of the asymmetry of the 3C-SiC crystal in which only (111) and $(\bar{1}\bar{1}1)$ slip planes are active out of the {111} family. © *2007 American Institute of Physics*. [DOI: 10.1063/1.2781324]

I. INTRODUCTION

Silicon carbide (SiC) is a highly desirable structural and electronic material. As a semiconductor, its performance in electronic devices for high-power, high-temperature, and high frequency applications is even better than silicon.[1,2] As to its outstanding mechanical properties, recent studies in both molecular dynamics (MD) simulations[3] and experiments[4] have shown that it can exhibit superhardness when the grain size is decreased to the nanometer regime. Lack of precise control over mechanical properties can lead to degradation of micro- and nanoscale electronic devices, and therefore it is essential to understand the mechanical properties at the atomistic level. Nanoindentation is an excellent technique for studies of elastic-plastic properties of thin films.[5–21] It was introduced by Oliver and Pharr[22] in 1992 for experimental determination of hardness and elastic modulus, and since then it has been widely adopted and verified.[22–25] Nanoindentation studies have focused on the onset of plasticity[26–29] and development of dislocation loops.[30–34] The elastic and plastic properties of materials under high pressure could result in amorphization and structural transformation.[35,36] In recent years, MD simulations have brought an atomic-level insight into the mechanisms of defect nucleation and their evolution during nanoindentation of thin films.[37–40] However, there are still many open questions concerning atomistic details of plastic flow during indentation. For example, Ning and Pirouz have investigated the core nature of partial dislocations in indentation-deformed cubic SiC and found that there is a morphology difference in Si core and C core.[41] Kaiser *et al.* have also investigated the behavior of partial dislocations and stacking faults in cubic SiC and they developed a procedure for determining the Burgers vector of possible types of dislocations.[41,42] However, the critical resolved shear stress for the onset of plastic flow has yet to be determined. Another outstanding question is related to pileup patterns formed on a surface after the unloading of the indenter. For example, Smith *et al.*[43] observed the pileup of atoms in Fe produced by dislocation loops that propagate in the inclined direction and cross slip between planes of the same family. Walsh *et al.*[38] observed amorphous pileup in silicon nitride pattern during nanoindentation. Wang *et al.*[44] have observed anisotropic pileup patterns in metals, and similar effects in ceramics are of interest.

In our previous nanoindentation simulation on 3C-SiC, we used a flat-punch indenter, where we observed amorphization.[45] This has raised an issue on the effect of the

[a)]Electronic mail: priyav@usc.edu

 © 2007 American Institute of Physics

Downloaded 19 Jun 2010 to 128.125.12.14. Redistribution subject to AIP license or copyright; see http://jap.aip.org/jap/copyright.jsp

indenter geometry. In this paper, we instead use a pyramidal-shaped Vickers and show that the indenter geometry, as well as the crystallographic orientation of the substrate, has important effects on the mechanical response. Here, we report multimillion-atom nanoindentation simulations of 3C-SiC on three surfaces coinciding with distinct crystallographic planes, (110), (001), and (111), using pyramidal-shaped Vickers indenter with 90° edge angle. SiC occurs in many different crystal structures, which can be distinguished by the stacking sequence of the silicon-carbon double layers.[46] The most common is the cubic polytype, zinc-blende structure denoted as 3C-SiC. We have investigated the correlation between load drops in the load-displacement curves and the nucleation of dislocations. We have found that plasticity in the simulated films is mediated by mutually repelling partial dislocations and to the extension of stacking faults, and that dislocations move in the glide-set planes. Through the analysis of the stress distribution, we have also determined the critical resolved shear stress necessary for the motion of dislocation lines. Furthermore, the anisotropy of the pileup patterns after unloading of the indenter shows strong correlations with the kinematics of dislocations on (111) and $(\bar{1}\bar{1}1)$ slip planes. We have observed that the anisotropic pileup patterns lie on (111) and $(\bar{1}\bar{1}1)$ slip planes for all three surface orientations under study.

This paper is organized as follows, Section II describes the simulation method, empirical interatomic potential, and its validation; simulation results are described in Sec. III; and finally, Sec. IV contains the conclusions.

II. INTERATOMIC POTENTIAL AND SIMULATION METHODOLOGY

MD simulations of nanoindentation in single crystal 3C-SiC have been performed with an interatomic potential developed by Vashishta *et al.*[47] The interatomic potential involves two-body and three-body terms,[48]

$$V = \sum_{i<j} V_{ij}^{(2)}(r_{ij}) + \sum_{i,j<k} V_{jik}^{(3)}(r_{ij}, r_{ik}), \tag{1}$$

where the two-body terms include the effects of steric repulsion, charge transfer between atoms, and charge-dipole and van der Waals interactions:

$$V_{ij}^{(2)}(r_{ij}) = \frac{H_{ij}}{r_{ij}^{n_{ij}}} + \frac{Z_i Z_j}{r_{ij}} e^{-r_{ij}/a} - \frac{D_{ij}}{r_{ij}^4} e^{-r_{ij}/b} - \frac{W_{ij}}{r_{ij}^6}. \tag{2}$$

In Eq. (2), H_{ij} and n_{ij} are parameters for steric repulsion, Z_i is the effective atomic charge for the Coulomb interaction, a and b are screening parameters, D_{ij} is the strength of charge-dipole interaction, and W_{ij} is a parameter in the induced dipole-dipole interaction. Three-body terms incorporate covalent effects through bond bending and bond-stretching terms:

TABLE I. Calculated and experimental values for selected physical properties of 3C-SiC.

	Experiments	MD
Lattice constant (Å)	4.3596[a]	4.3581
Cohesive energy (eV)	6.34[b]	6.3411
Melting/decomposition temperature (K)	3103±40[a]	3250±50
Bulk modulus (GPa)	225–270[a,c,d]	225.2
Elastic constants (GPa)		
C_{11}	390[d]	390.0
C_{12}	142[d]	142.6
C_{44}	150–256[a,d]	191.0

[a]Reference 67 (Ioffe).
[b]Reference 66 (Harrison).
[c]Reference 68 (Carnahan).
[d]Reference 69 (Feldman *et al.*).

$$V_{jik}^{(3)}(r_{ij}, r_{ik}) = B_{jik} \exp\left(\frac{\gamma}{r_{ij} - r_0} + \frac{\gamma}{r_{ik} - r_0}\right) \times \frac{(\cos\theta_{jik} - \cos\bar{\theta}_{jik})^2}{1 + C(\cos\theta_{jik} - \cos\bar{\theta}_{jik})^2} \times \Theta(r_0 - r_{ij})\Theta(r_0 - r_{ik}), \tag{3}$$

where B_{jik} is the strength of the interaction, $\Theta(x)$ is a step function, and γ, r_0, and $\bar{\theta}_{jik}$ are constants. Table I shows results for some of the physical properties calculated with this interaction potential and the corresponding experimental values. Parameters for the SiC interaction potential function are given by Vashishta *et al.*[48]

We have performed multimillion-atom MD simulation of nanoindentation on three 3C-SiC surfaces: (110), (001), and (111). The simulation box for the (110) surface nanoindentation is oriented in the $x[\bar{1}10]$, $y[001]$, and $z[110]$ directions; for the (001) surface, in the $x[100]$, $y[010]$, and $z[001]$ directions; and for the (111) surface, in the $x[\bar{1}10]$, $y[11\bar{2}]$, and $z[111]$ directions. The film dimensions in the three simulations are $592\times593\times197$ Å^3, $558\times558\times201$ Å^3, and $598\times592\times196$ Å^3, and contain 6 684 672, 6 029 312, and 6 709 248 atoms, respectively. Periodic boundary conditions are applied in the x and y directions, and the atomic positions in the bottom 12 Å layers are fixed. In all of the simulations, we used a four-faced pyramidal-shape rigid indenter with 90° edge angle, which is similar to the Vickers indenter. The base of the indenter is 141×141 Å^2 and the height is 100 Å. For simplicity, the interatomic interaction between the indenter and substrate is purely repulsive. The initial setup of the simulations is shown schematically in Fig. 1. The system is first thermalized at 300 K and this temperature is held constant during nanoindentation. The indenter is inserted into the film in steps of 0.5 Å. For each depth increment, the indenter is first pushed down at a speed of 1 Å/ps (a pushing phase). After each depth increment, the indenter is held fixed for 12–70 ps (a holding phase) until the force on the indenter reaches its asymptotic value within a prescribed tolerance. The indenter force is calculated as an average over two or three periods of force fluctuations characteristic for

Downloaded 19 Jun 2010 to 128.125.12.14. Redistribution subject to AIP license or copyright; see http://jap.aip.org/jap/copyright.jsp

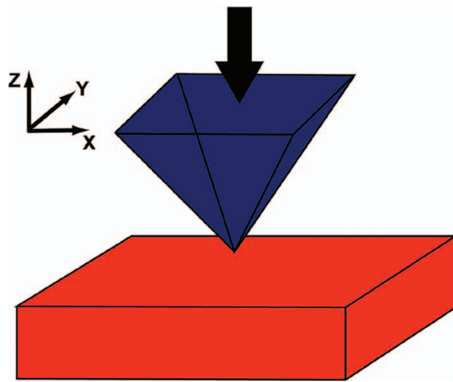

FIG. 1. (Color) Schematic view of the indenter/film system. For the three simulations, the film has dimensions of $592\times593\times197$ Å^3, $558\times558\times201$ Å^3, and $598\times592\times196$ Å^3 and 6 684 672, 6 029 312, and 6 709 248 atoms, respectively. For the (110) surface, x, y, and z are along $[\bar{1}10]$, [001], and [110] directions; for the (001) surface, they are along [100], [010], and [001] directions; and for the (111) surface they are along $[\bar{1}10]$, $[11\bar{2}]$, and [111] directions. The indenter is pushed along the z direction.

the holding phase. The total number of MD steps for each of the three simulations reported here is 4 440 500 with a MD time step of 2.0 fs.

III. RESULTS

A. Load-displacement curves and hardness

Indentation simulations can be examined through the analysis of the load-displacement (P-h) curve. Figure 2 shows the P-h curves for indentation of (110), (001), and (111) surfaces. These curves exhibit discrete load drops (pop-ins), which can be divided into two kinds: minor and major. Different crystallographic orientations result in load-drop events at different depths. For example, for the (110) surface, there are three major pop-in events at 30.5, 49.0, and 63 Å, respectively, during the loading process. Recent studies have shown that such pop-in events are often correlated with dislocation nucleation and interaction.[26–29,37,49,50] The presence of the hysteresis in the P-h curve in Fig. 2 (i.e., the discrepancy between the loading and unloading curves) indicates that plastic (irreversible) deformation has taken place in the indented films.

Nanoindentation testing provides information about the film's hardness. By definition, Vickers hardness (HV) is the load divided by the actual surface area of the residual impression.[51] With the 90° edge angle four-faced pyramidal-shaped indenter, the actual surface area as a function of indent depth h is given by

$$A = 3.464h^2. \tag{4}$$

In Fig. 3, HV has been plotted as a function of the indent depth for the three crystallographic directions. Despite its depth dependence, HV saturates at 26, 26.5, and 27.5 GPa for (110), (001), and (111) surfaces, respectively.

According to Cha *et al.*,[52] the microhardness tested by Vickers indenter for 3C-SiC thin film as grown by activated reactive evaporation process is between 17.2 and 36.1 GPa. Considering that the morphology of the experimental film is a little bit different from our simulation, our simulation results are in good agreement with this experiment.

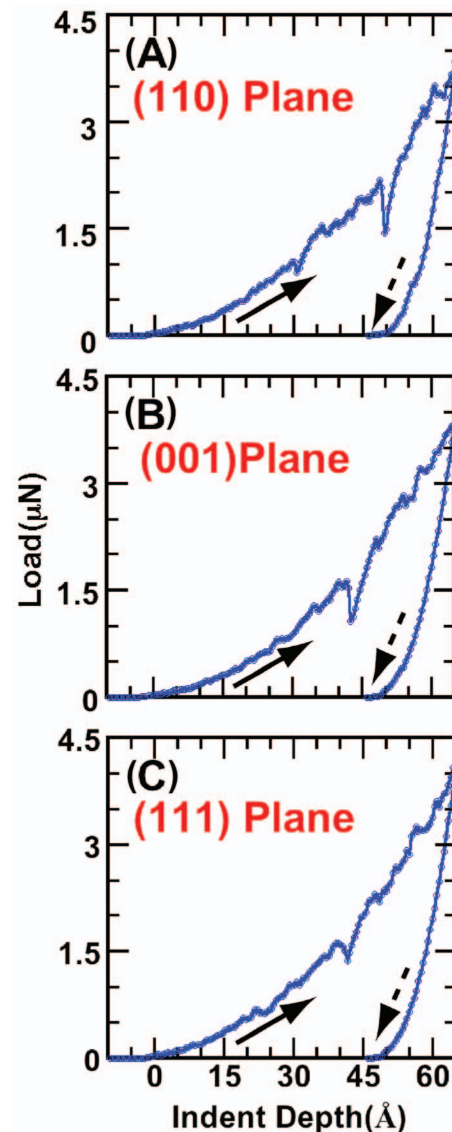

FIG. 2. (Color) Load-displacement (P-h) curves for (A) (110), (B) (001), and (C) (111) surfaces. The indentation response is different for the three crystallographic orientations. Solid and dashed arrows indicate the loading and unloading processes, respectively.

B. Dislocation activities

In order to examine plastic flow in the indented films, we employ the shortest-path ring analysis.[53,54] In a perfect 3C-SiC (zinc-blende) crystal, every atom has 12 shortest-path threefold rings.[55] Any atom for which the number of threefold rings is not 12 is imperfect. Atoms that have imperfect ring distributions depict the shape of dislocation loops, providing an effective tool for isolation and analysis of plastic events in the film during indentation. The most common slip system observed in 3C-SiC is [110] {111}, i.e., atoms are displaced along the [110] directions in one of the {111} planes.[56] Therefore a perfect dislocation in 3C-SiC has the $\frac{1}{2}\langle110\rangle$ Burgers vector. In our study, incipient plasticity oc-

Downloaded 19 Jun 2010 to 128.125.12.14. Redistribution subject to AIP license or copyright; see http://jap.aip.org/jap/copyright.jsp

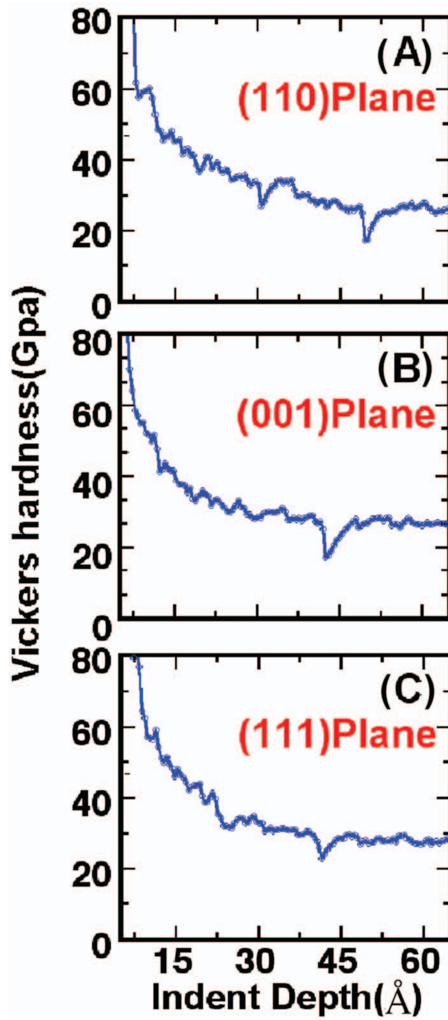

FIG. 3. (Color) Depth dependence of the hardness on (A) (110), (B) (001), and (C) (111) faces. The hardness converges to ~26, 26.5, and 27.5 GPa, respectively.

curs by nucleation of dislocations on the (111) plane, independently of the crystallographic direction of the indented surface.

During nanoindentation of the (110) surface, dislocations first appear as dissociated Shockley partials ($\frac{1}{6}\langle 112\rangle$ Burgers vector). Paired Shockley partial dislocations form hexagonal-shaped dislocation loops that enclose stacking faults (SFs) (see Fig. 4). Zinc-blende structure consists of two interpenetrating face-centered-cubic (fcc) lattices and therefore for the {111} slip systems, SFs can nucleate in two different plane sets: glide set and shuffle set.[57] For the glide-set SFs, dislocations reside on closely spaced planes, whereas for the shuffle-set stacking faults, the dislocations reside on widely spaced planes.[58] We find that glide-set Shockley partials move on a (111) slip plane by repelling each other. The area of the SF region therefore increases along with the motion of a dislocation loop. The Burgers vectors of Shockley partials obey

$$\tfrac{1}{6}[\bar{1}2\bar{1}]+\tfrac{1}{6}[\bar{2}11]=\tfrac{1}{2}[\bar{1}10]. \quad (5)$$

It has been known for years that 3C-SiC has partial dislocations and stacking faults.[42] Ning and Pirouz[41] have investigated the nature of dislocation cores in indentation-deformed 3C-SiC at high temperatures experimentally. Blumenau *et al.*[59] have performed quantum-mechanical calculations in the framework of the density functional theory to investigate the core nature of straight and kinked partial dislocations. However the Peierls stress, which controls the dislocation motions in 3C-SiC, has not been obtained. It is not known at what value of the resolved shear stress dislocations will move across the Peierls energy barrier. We calculate this value by resolving the stress onto the plane and direction on which the slip occurs. Consider a dislocation on (111) plane, which moves in the direction of $[\bar{1}\bar{1}2]$ (see Fig. 5). We transform the stress tensor from the original axes x,y,z ($[\bar{1}10],[001],[110]$) to x',y',z' ($[\bar{1}10],[\bar{1}\bar{1}2],[111]$), as illustrated in Fig. 5. The dislocation line we focus on is moving in the y' direction. Therefore, the shear stress that drives the dislocation line is $\tau_{z'y'}$.

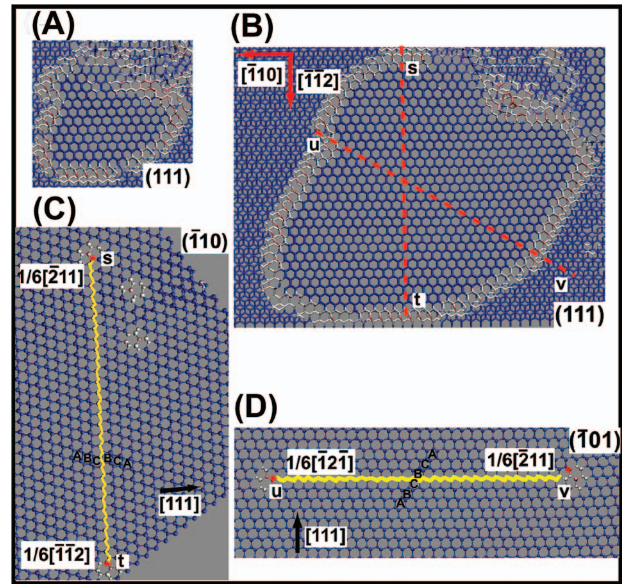

FIG. 4. (Color) Stacking fault (inner blue-color region) bounded by Shockley partial dislocations (white-colored atoms) at times (A) 0 ps and (B) 52 ps during holding phase at $h=30.5$ Å. Projection views are on (C) the $(\bar{1}10)$ and (D) the $(\bar{1}01)$, the intersections with the (111) plane of which are indicated by the line segments *st* and *u* in (B). The stacking of {111} layers is *ABCABC*, and (C) and (D) show an *ABCBCA* stacking fault across the yellow line. Burgers vectors and the directions of paired Shockley partials are indicated by red arrows. The slip plane is a glide-set plane between different stacking sequence layers.

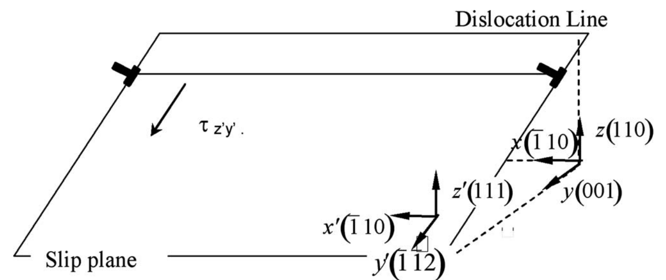

FIG. 5. Illustration of stress tensor transformation. The dislocation line is moving on a (111) slip plane in the $z'y'$ direction. We have performed stress tensor transformation from the original axes x,y,z ($[\bar{1}10],[001],[110]$) to x',y',z' ($[\bar{1}10],[\bar{1}\bar{1}2],[111]$) in order to investigate the critical shear stress that drives dislocation motion.

Downloaded 19 Jun 2010 to 128.125.12.14. Redistribution subject to AIP license or copyright; see http://jap.aip.org/jap/copyright.jsp

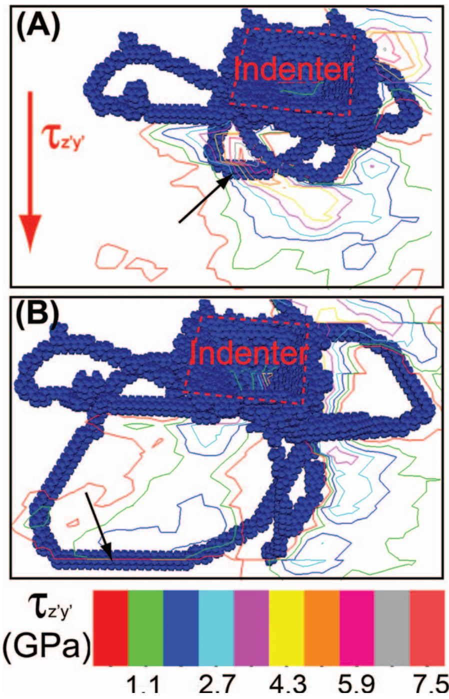

FIG. 6. (Color) Shear stress distribution on the (111) plane and dislocation loops detected by ring analysis at t=(A) 0 ps and (B) 52 ps during the holding phase for the first major pop-in event (h=30.5 Å) of (110) indentation. The indenter position is indicated by red dashed lines. Before dislocation movement (left), the stress contour is dense, and after $\tau_{z'y'}$, reaches 7.5 GPa, the straight dislocation line (indicated by black arrows) starts moving.

Figure 6 shows a color-coded contour of shear stress distribution $\tau_{z'y'}$ on (111) plane at times t=0 and 52 ps during the holding phase at h=30.5 Å, which corresponds to the first major pop-in event during nanoindentation of the (110) surface. Dislocation loops detected by ring analysis are also shown, where spheres are atoms that do not have 12 threefold rings. The movement of a dislocation line is indicated by the black arrow. By comparing Figs. 6(a) and 6(b), it can be seen that the maximum stress along the dislocation line decreases from 7.5 GPa at t=0 ps to around 2 GPa at t =52 ps.

Figure 7 shows the time evolution of the maximum shear stress acting on the dislocation line shown in Fig. 6, where t=0–0.5 ps is the pushing phase from h=30 to 30.5 Å and t=0.5–52 ps is the holding phase at h=30.5 Å. Stress relaxation due to the dislocation motion manifests itself as a sharp drop in the shear stress at ~10 ps. The shear stress dropped after the movement of the straight dislocation line (indicated by black arrows) and finally saturated at ~2 GPa. In order to estimate the Peierls stress, we average the shear stress along the atomistically straight dislocation segment of ~20 Å length just before it starts moving. The resulting estimate for the Peierls stress is 7.5 GPa$\approx 3.9\times 10^{-2}G$,[60] where G is the shear modulus (see Table I). Peierls stress as high as $10^{-2}G$ is consistent with values typically expected for covalent crystals. Figure 6 also shows that the shear stress contour becomes less dense with the motion of the dislocation line. After the indenter forces are fully relaxed (52 ps), the shear stress saturates around 2 GPa, since the motion of the dislocation line dissipates the accumulated energy.

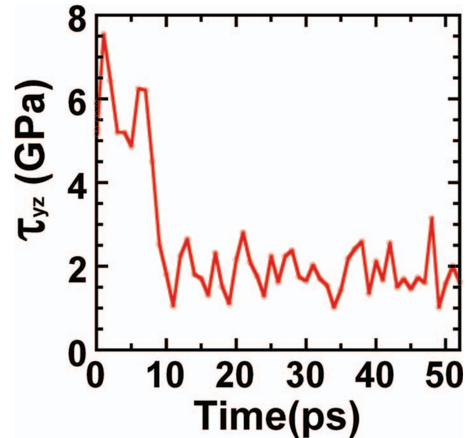

FIG. 7. (Color) The drop in shear stress with the onset of dislocation motion during the pushing (0–0.5 ps) and holding (0.5–52 ps) phases. Shown is the time evolution of the maximum shear stress on the dislocation line shown in Fig. 6.

Through a closer examination of dislocation motion, we find that the dislocation propagates by a kink-pair mechanism[58] at low stresses, as shown in Fig. 8. The initially straight dislocation line (indicated by the white dashed line) at 21 ps (A) moves one step further by nucleating a kink pair (denoted by black arrows) 1 ps later (B). The kink pair subsequently separates and moves toward the two ends of the dislocation line. At 23 ps, the dislocation line moves another step further by nucleating a new kink pair.

In addition to the above plastic deformation mechanism, we observe a cross-slip event between (111) and $(\bar{1}\bar{1}1)$ slip planes, as shown in Fig. 9. At h=20.75 Å (A), dislocations glide on the (111) slip plane. After indenting 0.5 Å deeper (B), the dislocation starts to glide on a $(\bar{1}\bar{1}1)$ plane. The cross product of (111) and $(\bar{1}\bar{1}1)$ is $(\bar{1}10)$, which is parallel to the Burgers vector of the perfect dislocation in SiC. It is known that cross slip occurs only for a screw segment of dislocation line, for which it is required that the cross product of the normal vectors of the two slip planes must be parallel to the Burgers vector. At h=22.24 Å (C), the dislocation goes back to (111) slip plane, leaving a ball-shaped sessile dislocation (marked by the red circle).

In order to examine the transition from Fig. 9(b) to Fig. 9(c) more closely, we plot in Fig. 10 the dislocation at t=2 (A) and 3 ps (B) during the holding phase of h=22.24 Å. The cross-slip mechanism is observed as the screw segment of the dislocation moves from $(\bar{1}\bar{1}1)$ back to (111) plane.

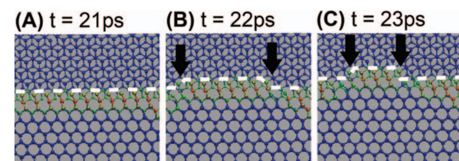

FIG. 8. (Color) (A) Kink-pair propagation (pointed by arrows) on a dislocation line (white dashed lines). (B) At 22 ps, a pair of kinks split and move toward the two ends of the dislocation line. (C) After 1 ps, another kink-pair is formed and follows the same mechanism as in (B). This moves the dislocation ahead.

Downloaded 19 Jun 2010 to 128.125.12.14. Redistribution subject to AIP license or copyright; see http://jap.aip.org/jap/copyright.jsp

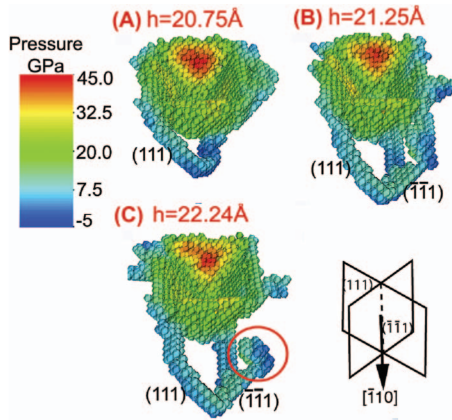

FIG. 9. (Color) Screw segments of the dislocation cross slip from (111) to $(\bar{1}\bar{1}1)$. Atoms with imperfect ring distributions are plotted for h=(A) 20.75 Å, (B) 21.25 Å, and (C) 22.24 Å, where the pressure is color coded. The red circle indicates a sessile dislocation.

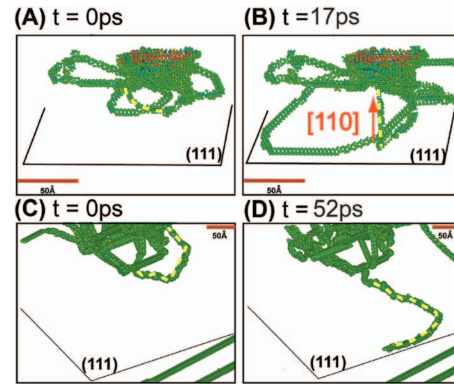

FIG. 11. (Color) Atoms with imperfect ring distributions are shown in t =(A) 0 ps and (B) 17 ps for h=30.5 Å (first major pop-in); t=(C) 0 ps and (D) 52 ps for h=49.5 Å (second major pop-in) during the holding phase. The indenter position is indicated by red dashed lines. The screw part of the dislocation (yellow dashed line) changes the slip plane from (111) (A) and lines up in [110] orientation (B) at the first major pop-in event of (110) indentation. In (C) and (D), the screw part of the dislocation line extends and opens up back to the (111) at the second major pop-in (h=49.5 Å) event of (110) indentation.

In order to examine the relation between indent depth and dislocation activities, in Fig. 11 we plot dislocation motion during the holding phase of the first two major pop-ins at h=30.5 Å [(A) and (B)] and at h=49.5 Å [(C) and (D)] observed during nanoindentation of the (110) surface. We can see that the dislocation loop is much more extended for the second major pop-in than in the first major pop-in. Also, the screw part of the dislocation line [marked by the yellow dashed line in (B)] moves from the (111) to a different slip plane and lines up in the [110] orientation and is more pronounced while the dislocation line [yellow dashed line in (C)] which is not contained in one single plane moves back to the (111) [yellow dashed line in (D)] at the second major pop-in than in the first major pop-in. These correlate with the fact that the magnitude of the load drop during the second major pop-in at h=49.5 Å (0.63 μN) is larger than that of the first pop-in at h=30.5 Å (0.15 μN). This confirms that plasticity mediated by dislocation motions is a source of energy dissipation associated with load drops.

In contrast to the nanoindentation of the (110) surface, when the (001) surface is indented, the first dislocation activity is a nucleation of perfect dislocations. For the indentation of the (111) surface, it is nucleation of partial dislocations, similarly to the (110) case. The pop-in events in the P-h curves all exhibit similar dislocation nucleation and motion that lead to energy dissipation.

C. Pileups

A pileup of material on a surface has been observed after unloading of the indenter for all three films under study (see Figs. 12–14). In recent studies, Wang *et al.*[44] described the orientation dependence of nanoindentation pileup patterns in a single crystal of copper. In their studies, experimental results are compared with those of a continuum-level model. Both techniques show the same pileup patterns on the surface. The observed pileup patterns are interpreted by the kinematics and dynamics of localized and crystallographic plastic flow. In our studies, we observe that the anisotropic pileup occurs on (111) and $(\bar{1}\bar{1}1)$ slip planes, as explained below.

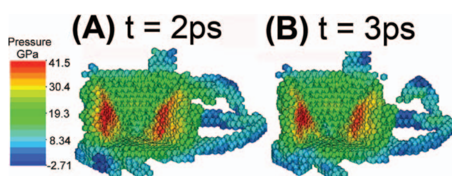

FIG. 10. (Color) Atoms with imperfect ring distributions are plotted for h =22.24 Å at t=(A) 2 ps and (B) 3 ps during the holding phase. After relaxation for 3 ps, the cross-slip mechanism disappears as dislocation moves from the $(\bar{1}\bar{1}1)$ plane to the (111) plane.

To analyze the pileup pattern, we calculate the distance

$$\xi_i = \|\mathbf{r}_i(\text{preloading}) - \mathbf{r}_i(\text{postloading})\| \tag{6}$$

for all atoms, where $\mathbf{r}_i$ is the position of atom i. Figure 12(a) shows a side view of the pileup pattern on the (110) surface, which is a cross section along the dashed line in Fig. 12(b). The colors indicate the displacement (ξ_i) of each atom from its position before indentation. The light blue color implies that the gliding distance of the (111) slip plane is equal to the Burgers vector of $a/2[\bar{1}10]$ perfect dislocations (a is the lattice constant) (3.08 Å); the red color shows the value of the Burgers vector of Shockley partials (1.78 Å); the purple color shows atoms that have moved more than the lattice constant of 4.36 Å. Figure 12(a) shows (111) and $(\bar{1}\bar{1}1)$ slips

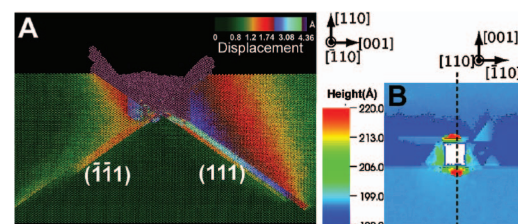

FIG. 12. (Color) (A) Side view of pileup of (110) indentation cut (dashed line) from the top view in (B). Colors indicate the displacement of each atom from its original position before indentation. (B) Surface morphology colored by height in the indent direction. Red color indicates the highest point of the pileup.

Downloaded 19 Jun 2010 to 128.125.12.14. Redistribution subject to AIP license or copyright; see http://jap.aip.org/jap/copyright.jsp

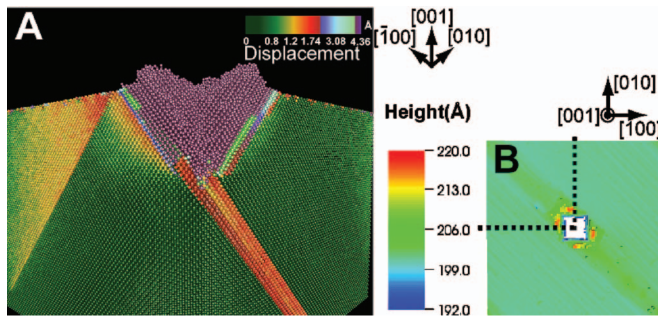

FIG. 13. (Color) (A) Cross cut along the dashed lines in (B) for the nanoindentation of the (001) surface. Colors show the atomic displacement due to indentation. Orange and red colors show the slip activities on slip planes. (B) Surface morphology of the (001) surface. Colors indicate the pileup region. Pileup pattern is aligned with slip systems.

and pileups at the intersections of the slip planes and (110) free surface. Figure 12(b) shows the surface morphology colored by height (indent direction). The red color indicates the highest point where the pileup resides. There are two major pileups: one on top of the indenter (white square), which corresponds to ($\bar{1}\bar{1}1$) slip, and the other below the indenter, which corresponds to (111) slip.

Figure 13 shows similar plots for the (001) surface. Figure 13(a) shows a side view of the pileup pattern corner cut from (001) film. Figure 13(b) shows four major pileups: two of them (top and right of the indenter, white square) correspond to ($\bar{1}\bar{1}1$) slip and the other two (below and left of the indenter) correspond to (111) slip. Figure 13(b) also shows a streak of dark green color along the diagonal from top left to bottom right, which corresponds to the direction of the Burgers vector of a perfect dislocation in [$\bar{1}$10].

If there are only two major slip planes, (111) and ($\bar{1}\bar{1}1$), in 3C-SiC, one should observe a onefold symmetry pileup pattern on the (111) surface. Since (111) is the direction of indentation, we should only see a pileup associated with the ($\bar{1}\bar{1}1$) plane. Indeed, a onefold symmetry of a pileup pattern is observed, as shown in Fig. 14 for the (111) surface nanoindentation. For example, Fig. 14(b) shows only one pileup marked in red on the left hand side of the indenter (white square). Figure 14(a) shows the center cut of the (111) film, where there is only one side of the pileup pattern, revealing the asymmetry of the 3C-SiC crystal.

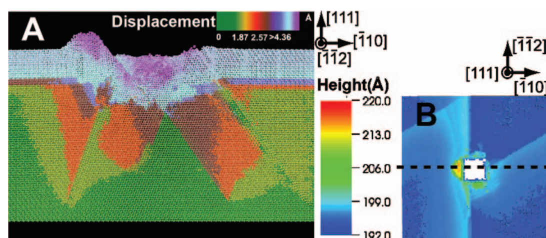

FIG. 14. (Color) (A) Center cut along the dashed line in (B) for the (111) film. Colors indicate an atomic displacement due to indentation. Since the (111) plane is one of the two slip planes, we only observe a onefold symmetry pileup pattern. (B) Surface morphology of the (111) surface. Colors show that the pileup pattern only resides on one side of the indenter.

IV. CONCLUSIONS

We have observed perfect dislocations, glide-set partial dislocations, and stacking faults on the {111} planes during nanoindentation along all three crystallographic directions. Also, we have examined the atomistic mechanisms of dislocation nucleation and motion and we have determined the Peierls stress for 3C-SiC (~ 7.5 GPa$\approx 3.9\times 10^{-2}G$). After dislocations start moving, they advance by a kink-pair mechanism. In most nanoindentation simulations in literature, the atomic positions of the bottom layers of the film are kept fixed, which suppresses the motion of dislocation networks. To minimize its effect on the simulation results, the largest indent depths in our simulations are made below 1/3 of the film thickness. Furthermore, in our analysis, we only consider dislocations above 100 Å, which are not affected by the constrained bottom in the film.[61] The maximum local hydrostatic pressure reached during all indentation simulations reported here is below 50 GPa, which is below the zinc-blende to rocksalt transformation pressure of 100 GPa reported by Shimojo *et al.*[62] The film indented on its (111) surface exhibits the highest hardness value calculated using the ideal area function for the indenter. We have observed anisotropic pileup patterns, which is a consequence of the asymmetry of the 3C-SiC crystal in which only (111) and ($\bar{1}\bar{1}1$) slip planes are active out of the {111} family. The pileup patterns for all three faces are closely correlated to the dislocation activities on (111) and ($\bar{1}\bar{1}1$) slip planes. Our work with 90° edge angle Vickers indenter shows no evidence of pressure-induced amorphization, which is in contrast to Szlufarska *et al.*[37] In Ref. 37, a flat-punch indenter on (110) 3C-SiC surface could not couple effectively with the two slip planes. The amorphization or the lack of it is likely related to different dislocation activities. Since the calculated Peierls barrier (stress required to move a dislocation) is in agreement with experiments, the dislocations are nucleated at the correct local value of stress in both simulations. The difference arises from the fact that the flat-punch indenter generates very large and localized shear stresses at the four corners of the indenter. The dislocations are generated from the four corners, and the amorphization process starts when dislocations meet. These dislocations pile up, i.e., they block each other from further slip on the {111} planes. The high local stress (due to the geometry of the indenter and due to the pileup) is evidenced by the fact that dislocations are able to cross slip on higher index planes, where they are much less mobile. The pileup of dislocations leads to an increased disorder in the sample and eventually to amorphization. The situation is different in the case of the diamond-shape indenter. Here, the shear stress is concentrated at the tip of the indenter, and even though the dislocations are generated at the same value of the local shear stress, they do not pile up in the same way as in the case of the flat-punch indenter. Dislocation pileup is absent in the case of the diamond-shape indenter, possibly because there is only one nucleation point (as compared to four in the flat-punch indenter), which reduces the degree of dislocation interactions. Also the {111} surfaces of the diamond indenter directly couple to the slip systems, whereas there is no direct coupling between the

Downloaded 19 Jun 2010 to 128.125.12.14. Redistribution subject to AIP license or copyright; see http://jap.aip.org/jap/copyright.jsp

surfaces of the flat-punch indenter and the slip planes. In the case of the diamond-shape indenter, dislocations are nucleated on {111} planes and they cross slip to other planes from the same family. Due to the lack of dislocation pileup, work hardening in this system is much less effective than under the flat-punch indenter and the resulting hardness is lower.

A common limitation of MD simulations is their short time scales. At zero temperature, an elastic limit criterion by Van Vliet *et al.*[28] allows conventional MD simulations to predict homogeneous dislocation nucleation, where the indentation rate does not play a significant role as long as it is less than the speed of sound.[63] However, the situation is more complex at finite temperatures, where thermal energy assists the system to cross the activation barriers of homogeneous and heterogeneous dislocation nucleations and propagations. The rates of these inelastic events can be expressed as a function of the activation energies according to the harmonic transition state theory,[63] and they give rise to different *P-h* responses at different indentation rates.[64,65] This issue will be addressed in our future works.

ACKNOWLEDGMENTS

This work was partially supported by AFOSR-DURINT, ARO-MURI, DOE-SciDAC, DTRA, and NSF. Numerical tests were performed at the University of Southern California using the 5384-processor Linux cluster at the Research Computing Facility and the 2048-processor Linux cluster at the Collaboratory for Advanced Computing and Simulations.

[1] J. B. Casady and R. W. Johnson, Solid-State Electron. **39**, 1409 (1996).
[2] C. E. Weitzel, J. W. Palmour, C. H. Carter, K. Moore, K. J. Nordquist, S. Allen, C. Thero, and M. Bhatnagar, IEEE Trans. Electron Devices **43**, 1732 (1996).
[3] I. Szlufarska, A. Nakano, and P. Vashishta, Science **309**, 911 (2005).
[4] F. Liao, S. L. Girshick, W. M. Mook, W. W. Gerberich, and M. R. Zachariah, Appl. Phys. Lett. **86**, 171913 (2005).
[5] D. F. Bahr, D. E. Kramer, and W. W. Gerberich, Acta Mater. **46**, 3605 (1998).
[6] D. F. Bahr and G. Vasquez, J. Mater. Res. **20**, 1947 (2005).
[7] D. F. Bahr, D. E. Wilson, and D. A. Crowson, J. Mater. Res. **14**, 2269 (1999).
[8] Y. L. Chiu and A. H. W. Ngan, Acta Mater. **50**, 1599 (2002).
[9] S. G. Corcoran, R. J. Colton, E. T. Lilleodden, and W. W. Gerberich, Phys. Rev. B **55**, R16057 (1997).
[10] W. W. Gerberich, J. C. Nelson, E. T. Lilleodden, P. Anderson, and J. T. Wyrobek, Acta Mater. **44**, 3585 (1996).
[11] W. W. Gerberich, S. K. Venkataraman, H. Huang, S. E. Harvey, and D. L. Kohlstedt, Acta Metall. Mater. **43**, 1569 (1995).
[12] A. Gouldstone, H. J. Koh, K. Y. Zeng, A. E. Giannakopoulos, and S. Suresh, Acta Mater. **48**, 2277 (2000).
[13] J. D. Kiely and J. E. Houston, Phys. Rev. B **57**, 12588 (1998).
[14] A. B. Mann and J. B. Pethica, Langmuir **12**, 4583 (1996).
[15] A. B. Mann and J. B. Pethica, Philos. Mag. A **79**, 577 (1999).
[16] T. A. Michalske and J. E. Houston, Acta Mater. **46**, 391 (1998).
[17] C. A. Schuh, Mater. Today **9**, 32 (2006).
[18] C. A. Schuh and A. C. Lund, J. Mater. Res. **19**, 2152 (2004).
[19] Y. Shibutani and A. Koyama, J. Mater. Res. **19**, 183 (2004).
[20] S. Suresh, T. G. Nieh, and B. W. Choi, Scr. Mater. **41**, 951 (1999).
[21] N. I. Tymiak, D. E. Kramer, D. F. Bahr, T. J. Wyrobek, and W. W. Gerberich, Acta Mater. **49**, 1021 (2001).
[22] W. C. Oliver and G. M. Pharr, J. Mater. Res. **7**, 1564 (1992).
[23] W. C. Oliver and G. M. Pharr, J. Mater. Res. **19**, 3 (2004).
[24] J. Thurn and R. F. Cook, J. Mater. Res. **17**, 1143 (2002).
[25] B. Bhushan, *Handbook of Micro/Nano Tribology* (CRC, Boca Raton, FL, 1999).
[26] E. B. Tadmor, R. Miller, R. Phillips, and M. Ortiz, J. Mater. Res. **14**, 2233 (1999).
[27] J. Li, K. J. Van Vliet, T. Zhu, S. Yip, and S. Suresh, Nature (London) **418**, 307 (2002).
[28] K. J. Van Vliet, J. Li, T. Zhu, S. Yip, and S. Suresh, Phys. Rev. B **67**, 104105 (2003).
[29] C. A. Schuh, J. K. Mason, and A. C. Lund, Nat. Mater. **4**, 617 (2005).
[30] G. B. Viswanathan, E. Lee, D. M. Maher, S. Banerjee, and H. L. Fraser, Acta Mater. **53**, 5101 (2005).
[31] Y. Gaillard, C. Tromas, and J. Woirgard, Philos. Mag. Lett. **83**, 553 (2003).
[32] T. F. Page, W. C. Oliver, and C. J. Mchargue, J. Mater. Res. **7**, 450 (1992).
[33] N. A. Stelmashenko, M. G. Walls, L. M. Brown, and Y. V. Milman, Acta Metall. Mater. **41**, 2855 (1993).
[34] K. A. Nibur and D. F. Bahr, Scr. Mater. **49**, 1055 (2003).
[35] B. B. Karki, L. Stixrude, and R. M. Wentzcovitch, Rev. Geophys. **39**, 507 (2001).
[36] R. M. Wentzcovitch, C. d. Silva, J. R. Chelikowsky, and N. Binggeli, Phys. Rev. Lett. **80**, 2149 (1998).
[37] I. Szlufarska, R. K. Kalia, A. Nakano, and P. Vashishta, Appl. Phys. Lett. **85**, 378 (2004).
[38] P. Walsh, R. K. Kalia, A. Nakano, P. Vashishta, and S. Saini, Appl. Phys. Lett. **77**, 4332 (2000).
[39] D. W. Brenner, S. B. Sinnott, J. A. Harrison, and O. A. Shenderova, Nanotechnology **7**, 161 (1996).
[40] S. B. Sinnott, R. J. Colton, C. T. White, O. A. Shenderova, D. Brenner, and J. Harrison, J. Vac. Sci. Technol. A **15**, 936 (1997).
[41] X. J. Ning and P. Pirouz, in *Silicon Carbide and Related Materials 1995* (Institute of Physics Publishing, Bristol, UK, 1996), Vol. 142, pp. 449–452.
[42] U. Kaiser, I. I. Khodos, M. N. Kovalchuk, and W. Richter, Crystallogr. Rep. **46**, 1005 (2001).
[43] R. Smith, D. Christopher, S. D. Kenny, A. Richter, and B. Wolf, Phys. Rev. B **67**, 245405 (2003).
[44] Y. Wang, D. Raabe, C. Kluber, and F. Roters, Acta Mater. **52**, 2229 (2004).
[45] I. Szlufarska, R. K. Kalia, A. Nakano, and P. Vashishta, Phys. Rev. B **71**, 174113 (2005).
[46] W. M. R. William and E. Lee, *Ceramic Microstructures-Property Control by Processing* (Springer, New York, 1994).
[47] P. Vashishta, R. K. Kalia, and A. Nakano, *Amorphous Insulators and Semiconductors* (Kluwer Academic, Dordrecht, the Netherlands, 1997).
[48] P. Vashishta, R. K. Kalia, A. Nakano, and J. P. Rino, J. Appl. Phys. **101**, 103515 (2007).
[49] J. E. Bradby, J. S. Williams, J. Wong-Leung, M. V. Swain, and P. Munroe, Appl. Phys. Lett. **78**, 3235 (2001).
[50] J. E. Bradby, J. S. Williams, and M. V. Swain, Phys. Rev. B **67**, 085205 (2003).
[51] A. C. Fischer-Cripps, *Nanoindentation* (Springer, New York, 2004).
[52] Y. C. Cha, G. Kim, H. J. Doerr, and R. F. Bunshah, Thin Solid Films **253**, 212 (1994).
[53] S. R. Kalidindi, C. A. Bronkhorst, and L. Anand, J. Mech. Phys. Solids **40**, 537 (1992).
[54] C. Zhang, B. Bansal, P. S. Branicio, R. K. Kalia, A. Nakano, A. Sharma, and P. Vashishta, Comput. Phys. Commun. **175**, 339 (2006).
[55] J. P. Rino, I. Ebbsjo, R. K. Kalia, A. Nakano, and P. Vashishta, Phys. Rev. B **47**, 3053 (1993).
[56] R. Stevens, J. Mater. Sci. **7**, 517 (1972).
[57] W. Cai, V. V. Bulatov, J. Chang, J. Li, and S. Yip, *Dislocation Core Effects on Mobility* (North-Holland, Amsterdam, 2004), Vol. 12.
[58] J. P. Hirth and J. Lothe, *Theory of Dislocations* (Wiley, New York, 1982).
[59] A. T. Blumenau, C. J. Fall, R. Jones, M. I. Heggie, P. R. Briddon, T. Frauenheim, and S. Oberg, J. Phys.: Condens. Matter **14**, 12741 (2002).
[60] We have estimated the finite-size effect on the calculated shear stress as follows. For a straight dislocation segment of length l with its vertical bending bounded by Δ, the lower bound for the radius of curvature is estimated as $R_{lb}=(\Delta^2+l^2)/4\Delta$. The corresponding upper bound for the restoring stress is $\sigma_{up}=Gb/R_{lb}=2.4$ GPa, for the measured values of $l=20$ Å and $\Delta=0.7$ Å in the present case.
[61] I. Szlufarska, Mater. Today **9**, 42 (2006).
[62] F. Shimojo, I. Ebbsjo, R. K. Kalia, A. Nakano, J. P. Rino, and P. Vashishta, Phys. Rev. Lett. **84**, 3338 (2000).
[63] A. Gouldstone, N. Chollacoop, M. Dao, J. Li, A. M. Minor, and Y.-L. Shen, Acta Mater. **55**, 4015 (2007).
[64] P. C. Wo, L. Zuo, and A. H. W. Ngan, J. Mater. Res. **20**, 489 (2005).

Downloaded 19 Jun 2010 to 128.125.12.14. Redistribution subject to AIP license or copyright; see http://jap.aip.org/jap/copyright.jsp

[65]J. K. Mason, A. C. Lund, and C. A. Schuh, Phys. Rev. B **73**, 054102 (2006).
[66]W. A. Harrison, *Electronic Structure and the Properties of Solids: The Physics of the Chemical Bond* (Freeman, San Francisco, 1980).
[67]Ioffe Institute, 2003 (http://www.ioffe.ru/SVA/NSM/).
[68]R. D. Carnahan, J. Am. Ceram. Soc. **51**, 223 (1968).
[69]D. W. Feldman, J. H. Parker, W. J. Choyke, and L. Patrick, Phys. Rev. **173**, 787 (1968).

Downloaded 19 Jun 2010 to 128.125.12.14. Redistribution subject to AIP license or copyright; see http://jap.aip.org/jap/copyright.jsp